

Unblockable Communication With Gravity

Andrew J. Groszek  ^{1,2,*} Charles W. Woffinden  ^{1,2,†} Michael D. Harvey  ^{2,3} Andrew G. White  ² and Matthew J. Davis  ^{2,‡}

¹*These authors have contributed equally to this work and share first authorship.*

²*Australian Research Council Centre of Excellence for Engineered Quantum Systems, School of Mathematics and Physics, University of Queensland, St. Lucia, QLD 4072, Australia.*

³*Quantum Australia, School of Mathematics and Physics, University of Queensland, St. Lucia, QLD 4072, Australia.*

All modern wireless communication technologies are based on electromagnetism. However, electromagnetic signals are susceptible to screening and blocking, so their availability cannot be guaranteed in adverse environments. This raises a fundamental question: Can information be transmitted through a truly unblockable channel? Here we show that gravity, unlike electromagnetism, offers such a path. We propose and implement a wireless communication protocol in which a broadcaster encodes a binary message by moving a mass, while a receiver detects the resulting gravitational signal with a gravimeter. We validate this scheme experimentally, successfully transmitting a gravitational message a distance of ≈ 0.7 m through a brick wall at a rate of 1 bit min^{-1} . These results establish gravity as a viable platform for unblockable communication.

Suppose Alice is confined to a perfectly shielded room: no photons, sound waves, particles, or thermal signals can enter or escape. If Bob is outside the room, is there any physical mechanism Alice can use to communicate with him? The answer is yes—she can use gravity. Since all observed mass is strictly positive [1, 2], no known material can shield against gravitational fields [3]. So if Alice moves a mass within the room, the local gravitational field at Bob’s location will inevitably change, and this effect can be detected using a gravimeter. Alice can therefore communicate with Bob by encoding information in the gravitational field. In the simplest scenario, Alice can generate a binary gravitational signal by moving the mass between two positions (Fig. 1).

This unblockable wireless communication scheme stands in contrast to conventional methods based on electromagnetic waves, as these can be blocked by Faraday cages, and attenuate when passing through matter [4]. Near-unblockable communication has previously been proposed using neutrinos [5] and gravitational waves [6], but these approaches are somewhat hindered by the difficulty in generating a measurable signal—e.g. requiring the manipulation of black holes—as well as the prohibitively large detectors required [5, 7]. Gravitational communication, on the other hand, can be realised

with a mass and an off-the-shelf, hand-held gravimeter. For example, if Alice has access to a 100 kg mass, and moves it from 1 m to 2 m away from Bob, the expected change in gravitational acceleration at Bob’s location is $\sim 5 \text{ nm s}^{-2}$ [see Eq. (1)]. While this change may go unnoticed by the casual observer, Bob’s gravimeter is capable of detecting it.

Off-the-shelf gravimeters, typically based on mass-spring [8–10] or falling-corner-cube [11] designs, can provide sensitivities of $\sim 1 \text{ nm s}^{-2}$ [12]. Higher precisions of $\sim 0.01 \text{ nm s}^{-2}$ can be reached with superconducting gravimeters [12, 13], although at a cost of portability and price. Emerging gravimetry platforms—such as cold-atom interferometry [14, 15], optically levitated nanospheres [16, 17], and microelectromechanical systems devices [18–20]—promise even higher precision or low-cost alternatives in the near future. These advances may unlock a range of previously inaccessible technologies, such as detecting contraband materials [21] and underwater objects [22], or constructing gravimetry networks for early-warning earthquake detection [23]. It is therefore an opportune time to consider the possibility of gravitational communication.

Here, we first explore the theoretical properties of gravitational communication, including signal strengths, broadcast directionality, data rates, and robustness. We then experimentally demonstrate this scheme by broadcasting a gravitational message using an elevator counterweight, with an off-the-shelf spring-based gravimeter used for detection.

Signal generation—Our proposed gravitational communication scheme is purely classical, and can therefore be described by Newton’s law of gravitation. If Alice holds a point mass M at position \mathbf{r} , the gravitational acceleration it creates at Bob’s detector (assumed to be at the origin) is

$$\mathbf{g}(\mathbf{r}) = \frac{GM}{r^2} \hat{\mathbf{r}}, \quad (1)$$

where G is the gravitational constant. As Alice moves her mass between two positions, \mathbf{r}_0 and \mathbf{r}_1 , this gravitational acceleration changes by $\Delta \mathbf{g} = \mathbf{g}(\mathbf{r}_1) - \mathbf{g}(\mathbf{r}_0)$, generating a signal

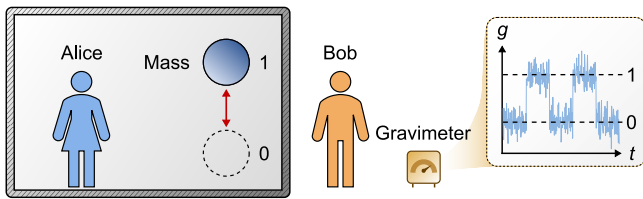


Figure 1. Schematic of gravitational communication. Alice (inside a perfectly shielded room) can communicate with Bob (outside the room) by moving a mass between two positions ‘0’ and ‘1’ to create a binary change in the local gravitational field. The inset shows a schematic of the gravitational acceleration g measured with Bob’s gravimeter as Alice moves the mass between the two positions.

for Bob to measure.

According to Eq. (1), the largest signal that Alice can theoretically generate is $|\Delta g| = GM/d^2$, assuming she is constrained to one side of the sensor (as in Fig. 1), and that the room is large enough for her to move the mass from some initial distance $r_0 = d$ to a much greater $r_1 \gg d$. However, if Bob's gravimeter—like many off-the-shelf gravimeters—only measures the vertical component of gravity g_z , the maximum signal will decrease. In the best case, Alice can still achieve $|\Delta g_z| \approx 0.8GM/d^2$, provided she is able to move the mass between vertical positions $z_{\pm}^* \approx \pm 0.7d$ (details of this calculation can be found in the Supplemental Material [24]). Geometric effects can therefore be largely mitigated, but only by displacing the mass over a distance on the order of the transmission length.

Directional properties—By moving the mass between her two chosen positions, Alice has created a gravitational antenna. To understand this antenna's properties, we consider a point mass moved vertically between $+\Delta z$ and $-\Delta z$, as illustrated in Fig. 2(a), and a single z -axis gravimeter as the detector, located at polar position $\mathbf{r} = (r, \alpha)$. Figure 2(b) shows a series of normalised polar plots of the change in gravitational signal as a function of the gravimeter's angular position α for multiple radii r (denoted by the legend). For mathematical details, see the Supplemental Material [24].

For $r/\Delta z \ll 1$, the signal is independent of α , and hence the antenna is omnidirectional for an observer near its centre. As $r/\Delta z$ approaches unity, the signal becomes increasingly directional along the z -axis, due to the increasing proximity of the gravimeter to the mass at $\alpha = 0^\circ$ and $\alpha = 180^\circ$ (note that the signal diverges at $r/\Delta z = 1$ when the two coincide). Further increasing r leads to the far-field regime ($r/\Delta z \gg 1$), where the antenna's transmission broadens again, but remains primarily directed along its axis.

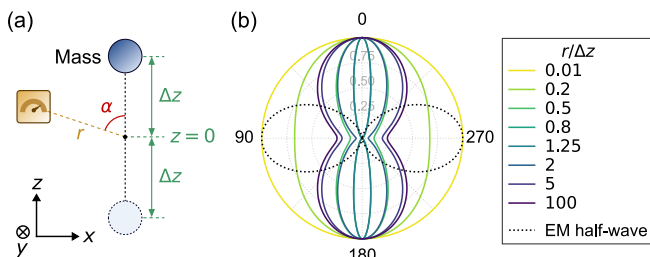


Figure 2. (a) Schematic of a point mass moving between vertical positions $+\Delta z$ and $-\Delta z$, forming a gravitational dipole antenna. The gravimeter, at position (r, α) in the xz -plane, measures a change in gravitational field as the mass moves between the two positions. (b) Polar plots of the vertical signal Δg_z from the gravitational antenna, as a function of the polar angle α from the axis of the antenna. Line colours denote the radial distance $r/\Delta z$ from the centre of the antenna, indicated by the legend. The strength of the signal at each radius is normalised to the largest value at that radius. For comparison, an electromagnetic half-wave dipole antenna radiation pattern is shown as a black dotted line. Note that all patterns are symmetric with respect to rotation around the z -axis.

For comparison, we show the far-field radiation pattern of an electromagnetic (EM) half-wave dipole antenna [25] [dotted line Fig. 2(b)]. This looks broadly similar to the gravitational antenna's far-field signal, except for a rotation by 90° relative to the antenna's axis. However, the gravitational antenna transmits at 0.25 of its maximum perpendicular to its two lobes in the far-field, whereas the dipole EM antenna has zero transmission in the perpendicular directions. Despite the similarities between the radiation patterns, we emphasise that the two physical scenarios are quite different: EM antennas rely on flowing currents to generate EM waves, whereas gravitational antennas create a change in a static field, more akin to a static electric dipole. Accordingly, the gravitational antenna signal decays with distance as $\sim r^{-3}$ [24], compared to the $\sim r^{-1}$ decay of an EM antenna [4].

Data rate—A key property of any communication channel is the maximum rate of error-correctable data transfer it allows, known as its capacity C . For a noisy digital channel, the Shannon–Hartley theorem [26] gives $C = (f_t/2) \log_2(1 + \text{SNR})$, with f_t the bit transmission frequency and SNR the signal-to-noise ratio. Here we take $f_t = 1/(T + \tau)$, where T is the time it takes Alice to move the mass between positions 0 and 1, and τ is the integration time of Bob's measurement. Assuming the noise is Gaussian, the SNR will grow as $\approx (f_s \tau)^{1/2}$ for sampling frequency f_s . For a gravitational signal from a point mass, the SNR will also decay with distance r as $\text{SNR}_{\text{ss}}(r/r_0)^{-2}$, where SNR_{ss} is the single-shot SNR at some reference distance r_0 . Putting this all together, the channel capacity for binary gravitational communication can be written:

$$C = \frac{1}{2(T + \tau)} \log_2 \left[1 + \text{SNR}_{\text{ss}} \frac{\sqrt{f_s \tau}}{(r/r_0)^2} \right]. \quad (2)$$

In the regime where the signal is easily resolvable (i.e. $\text{SNR} \gg 1$), the logarithmic term varies slowly with both integration time τ and distance r , and hence the prefactor dominates the scaling. In this limit, reducing r therefore makes little difference to the channel capacity—it is ultimately limited by $T + \tau$, and would most efficiently be increased by reducing these two timescales as much as possible. Conversely, in the limit of near-zero signal, $\text{SNR} \lesssim 0$, the channel capacity reduces to $C \sim \tau^{1/2}/(T + \tau)$. This function is maximised at $\tau = T$, so reducing τ below this value actually leads to a reduction in the channel capacity, despite increasing the bit rate.

Robustness—While this communication method cannot be blocked, it can be impacted by other active signal degradation methods. A malicious actor, Mallory, could jam Alice's signal by moving other nearby masses, making it difficult for Bob to decipher the message. Mallory could also spoof the signal (i.e. produce false 0 or 1 readings), although this would be much more difficult: they would require a second nearby object (unbeknownst to Bob) with a mass, distance and direction chosen to give the same sensor reading as Alice's true mass. Bob can mitigate both types of attack by using a three-axis sensor to measure the full vector $\Delta \mathbf{g}$ [24]. Opting for a less sophisticated approach, Mallory could attempt to disrupt Bob's

measurement by accelerating the gravimeter in other ways, such as vibrating the ground or even the air around the sensor. Bob could thwart such attacks using vibration isolation techniques.

Experiment—We experimentally demonstrate the proposed method of communication by transmitting a gravitational message through a wall from the elevator shaft into an adjacent room using a movable elevator counterweight. The change in gravitational field is detected at a nearby location with an off-the-shelf sensor. Specifically, we use a LaCoste and Romberg Model D mass–spring gravimeter, which measures relative changes in the vertical component of the gravitational field [27]. It has a data acquisition rate of ≈ 1.9 Hz, digital resolution of 10 nm s^{-2} , and an in-built low-pass filter with a 40 s window for removing high frequency noise. We have measured its sensitivity in the experimental location to be $\sim 2 \text{ nm s}^{-2}$ after ~ 30 s of averaging [24].

The sensor was placed on the ground floor, separated from the counterweight by a brick wall that blocks acoustic, optical and near-infrared communication [see Fig. 3(a)]. As the counterweight moves vertically, there is a change in the vertical gravitational acceleration g_z at the gravimeter’s location. This change, schematically depicted in Figure 3(b) as a function of the counterweight’s vertical position z , allowed us to encode a binary message in the movement of the mass as it transited between the lower and upper floors (as in Fig. 1).

To maximise the signal for the demonstration, we placed the gravimeter as close as possible to the counterweight, at horizontal distances $\Delta x = 0.56(3)$ m and $\Delta y = 0.00(5)$ m from the gravimeter’s centre to the counterweight centre of mass (COM). We estimated the counterweight’s COM to be $z_0 = 0.39(6)$ m above the gravimeter in the lower (0) position, and $z_1 = 5.80(6)$ m above it in the upper (1) position (see Fig. 3).

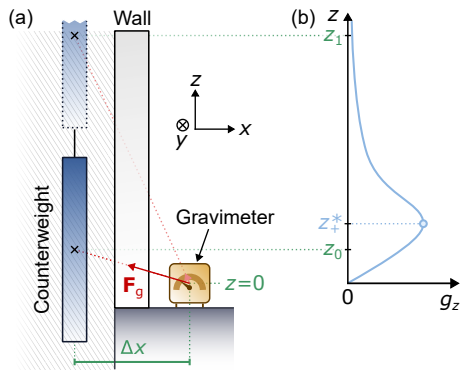


Figure 3. Schematic of experimental setup (not to scale). (a) The counterweight in the lower (0) and upper (1; dotted boundary) position. The force \mathbf{F}_g on the gravimeter’s test mass due to the gravitational attraction to the counterweight changes in both magnitude and direction between the two positions, as indicated. (b) Schematic of the expected vertical gravitational signal g_z , as a function of the counterweight’s vertical position. The lower and upper counterweight positions are indicated as z_0 and z_1 , respectively. The maximal vertical signal occurs at an intermediate height z_* , resulting from the tradeoff between the directionality of the sensor and $\sim z^{-2}$ fall-off of gravity.

The COM of the counterweight was therefore a distance of $0.68(4)$ m away from the sensor in its closest position, which we define as the range of the communication scheme. We also estimated the counterweight’s mass to be $1800(200)$ kg. The Supplemental Material [24] contains further details regarding these measurements.

We constructed a model of this setup, approximating the counterweight as a rectangular prism of uniform density. Using an integral form of Newton’s law of gravitation, we calculated the vertical gravitational signal g_z at the location of the sensor, as a function of the model counterweight’s vertical position [Fig. 3(b) shows a schematic of the result; see the Supplemental Material for details [24]]. The model predicts a change in g_z of $50(15) \text{ nm s}^{-2}$ as the counterweight moves between the upper and lower positions, which we expect to be resolvable with our gravimeter. The model further suggests that a $\approx 70\%$ signal boost would be achievable by optimising the counterweight position such that $z_0 = z_*$ [see Fig. 3(b)].

We began the experiment by vertically aligning the gravimeter using its built-in spirit levels, followed by ≈ 20 minutes of settling time. We then started acquiring data, leaving the elevator counterweight in the lower position for ≈ 25 minutes to obtain a background measurement. Following this, we transmitted a gravitational sequence of nine 7-bit ASCII characters by moving the elevator counterweight between its two positions in a chosen sequence. The bits were sent at a rate of one per minute, allowing for the ≈ 25 s counterweight movement time, followed by 10 s settling time, and 25 s of integration time. We chose to transmit the word ‘Gravity’, which is expressed as 49 bits: 1000111 1110010 1100001 1110110 1101001 1110100 1111001. We also included a control sequence of seven alternating bits (1010101) both before and after the message, to delineate the signal from the background and establish the transmission bit rate the receiver should expect. After the bit sequence, we acquired an additional ≈ 20 minutes of background (with the counterweight returned to its lower position) in order to quantify measurement drift [24].

The gravitational signal g_z detected by the gravimeter over the course of the experiment is shown in Fig. 4. Note that these data have been corrected for both Earth tide and sensor drift [24]. Each character is delineated with vertical dashed lines, and each bit with alternating background shading. The horizontal solid lines indicate the mean g_z value measured over that time window. Evidently, the data show distinct shifts of $\approx 50 \text{ nm s}^{-2}$ each time the elevator counterweight is moved, consistent with the prediction of our model. While there are small fluctuations in the mean values, the averaged 0 and 1 signals are clearly distinguishable, and the detected bit sequence exactly matches the original transmission. For comparison, a dotted horizontal line is shown in Fig. 4 at 25 nm s^{-2} , approximately halfway between the two bit values. Even without averaging, the bit error rate of individual measurements (i.e. the probability of a bit flipping by crossing the threshold) is already ≈ 0.01 . After averaging, this value reduces to $\approx 10^{-9}$ (assuming Gaussian fluctuations), comparable to fibre optic error rates [28]. We have thus successfully trans-

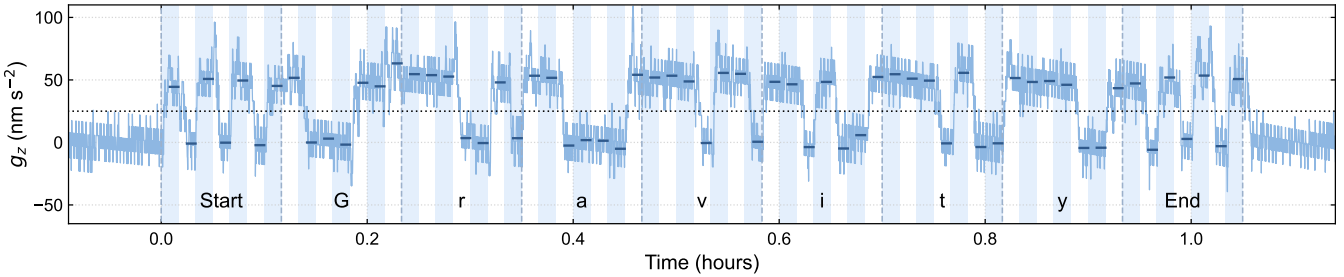


Figure 4. Gravimetry signal g_z over the transmission sequence (corrected for tide and drift [24]). The start and end points of each 7-bit ASCII character are denoted with vertical dashed lines. The 60 s temporal window for each bit is indicated by the alternating blue and white shading, and horizontal solid lines show the corresponding mean g_z for that interval, where the average is taken over the final 25 s. All measurements above (below) $g_z = 25 \text{ nm s}^{-2}$ (horizontal black dotted line) after correction are recorded as a 1 (0). Note that this is a relative gravitational measurement, and hence the offsets of the data are arbitrary. The sign convention of the data is such that a positive change in g_z corresponds to an increase in downward acceleration.

mitted and received a message via the gravitational field [29].

Potential improvements—Our experiment achieved a data transfer rate of 1 bit min^{-1} . The channel capacity for our experimental parameters is $\approx 2.4 \text{ bit min}^{-1}$, so in principle improvements could be made to the scheme by implementing more efficient encoding methods, e.g. phase shift keying [30]. This optimal information rate is limited by a number of factors, such as the slow movement of the elevator, and the 40 s low-pass filter integrated within the gravimeter. If our building had a modern elevator with a transition time of 5 s, and we had access to the latest Scintrex CG-6 gravimeter [31], the channel capacity would increase to $\approx 15 \text{ bit min}^{-1}$ (assuming an integration time of 0.1 s for a single sample, with SNR ≈ 5 [32]). However, improvements beyond this would be challenging, given that the mass movement time is the limiting factor.

While the data rate cannot be increased much beyond that demonstrated, the communication range can in principle be improved significantly. Table I lists a number of optimisations that could be made, as well as their expected improvement factor for the range, based on Eq. (1). Firstly, the configuration could be modified by compressing the mass into a more spatially localised geometry (ideally, a sphere), and vertically aligning it with the gravimeter. These changes would increase the signal by a factor of ≈ 4.9 at the same distance of $\approx 0.7 \text{ m}$. The mass itself could be increased within reason to, e.g. $7.5 \times 10^4 \text{ kg}$ (equivalent to a typical military tank [33]). An order of magnitude of SNR could also be sacrificed in favour of range, and in principle a higher sensitivity gravimeter could be used (e.g. a superconducting device [12, 13], or potentially a future cold-atom interferometer [34, 35]). Our experimental model predicts that sacrificing SNR (the only option available

with our current setup) could increase the potential range to $\approx 1.7 \text{ m}$. Combining all the improvements listed in Table I, we predict that the range could be increased by a factor of ~ 700 to $\sim 500 \text{ m}$.

Clearly, even with these idealised improvements, the scheme has a low data rate and short range when compared to other use cases. For example, the transmission rate for uplink commands to the Voyager 1 spacecraft—the furthest human-made object from Earth at $\sim 10^{13} \text{ m}$ away—is a significantly higher $\approx 960 \text{ bit min}^{-1}$ [36] (although being electromagnetic, this signal is inherently susceptible to jamming and blocking). We therefore expect gravitational communication to be best suited to the transmission of concise messages over relatively short distances in challenging or constrained environments.

Conclusion—We have proposed a form of unblockable communication using classical gravitation, and performed a proof-of-principle experimental demonstration. Using an elevator counterweight and an off-the-shelf gravimeter, we have successfully transmitted a gravitational message.

Although this technology is restricted to relatively short-range, low bit-rate applications, its unique advantages may be relevant for some niche use cases. Since it is possible to measure gravitational fields without the need for electronics [27, 37] (akin to semaphore), this approach could be made radiation-proof; however, unlike semaphore, it is not limited by line of sight. A scheme similar to that demonstrated here would be well-suited to communication from within secure facilities in a covert manner, which could be considered to prevent data leaks. There may also be potential applications enabling wireless communication to or from sealed nuclear bunkers. Should the reader ever experience prolonged entrapment in a soundproofed, Faraday-caged elevator with a malfunctioning phone, the present method offers an experimentally verified means of signalling for aid.

Acknowledgements—Funding for this work was provided by Australian Research Council Centre of Excellence for Engineered Quantum Systems (EQUS, CE170100009), and the Australian government Department of Industry, Science, and Resources via the Australia-India Strategic Research Fund

Table I. Potential improvements to transmission range.

	Current	Potential	Range increase factor
Geometric factor	1	≈ 4.9	≈ 2.2
Mass (kg)	1800	75 000	≈ 6.5
Sensitivity (nm s^{-2})	≈ 2	≈ 0.01	≈ 14
SNR	≈ 25	≈ 2	≈ 3.5

(AIRXIV000025). We thank Geoscience Australia for the loan of the gravimeter and for their technical advice, as well as Guillaume Gauthier, Charlotte Thomson and Lewis Williamson for comments on the manuscript. AGW wishes to thank Paulo Nussenzveig for conversations musing on applications of next generation quantum technologies.

* a.groszek@uq.edu.au
 † c.woffinden@uq.edu.au
 ‡ mdavis@uq.edu.au

[1] R. Schoen and S.-T. Yau, *Communications in Mathematical Physics* **65**, 45 (1979).

[2] N. de Aguiar Alves, A. G. S. Landulfo, and B. A. Costa, *Physical Review D* **111**, 044027 (2025).

[3] C. S. Unnikrishnan and G. T. Gillies, *Physical Review D* **61**, 101101 (2000).

[4] D. J. Griffiths, *Introduction to Electrodynamics* (Cambridge University Press, 2023).

[5] D. D. Stancil, P. Adamson, M. Alania, L. Aliaga, M. Andrews, *et al.*, *Modern Physics Letters A* **27**, 1250077 (2012).

[6] H. Wang and O. B. Akan, *IEEE Communications Surveys and Tutorials*, 1 (2025).

[7] B. P. Abbott, R. Abbott, T. D. Abbott, M. R. Abernathy, F. Acernese, K. Ackley, C. Adams, T. Adams, *et al.*, *Physical Review Letters* **116**, 061102 (2016).

[8] J. M. Goodkind, *Review of Scientific Instruments* **70**, 4131 (1999).

[9] M. Van Camp, O. de Viron, A. Watlet, B. Meurers, O. Francis, and C. Caudron, *Reviews of Geophysics* **55**, 938 (2017).

[10] S. K. Haldar, *Mineral Exploration*, 2nd ed. (Elsevier, 2018) Chap. 5.

[11] T. Niebauer, in *Treatise on Geophysics*, edited by G. Schubert (Elsevier, Amsterdam, 2007) pp. 43–64.

[12] W. Freedon, Gravimetry, in *Decorrelative Mollifier Gravimetry: Basics, Ideas, Concepts, and Examples* (Springer International Publishing, Cham, 2021) pp. 41–48.

[13] H. Virtanen, *Studies of earth dynamics with the superconducting gravimeter*, Ph.D. thesis, Finland (2006).

[14] M. Kasevich and S. Chu, *Applied Physics B* **54**, 321 (1992).

[15] X. Wu, Z. Pagel, B. S. Malek, T. H. Nguyen, F. Zi, D. S. Scheirer, and H. Müller, *Science Advances* **5**, eaax0800 (2019).

[16] F. Monteiro, W. Li, G. Afek, C.-l. Li, M. Mossman, and D. C. Moore, *Physical Review A* **101**, 053835 (2020).

[17] T. Dinter, R. Roberts, T. Volz, M. K. Schmidt, and C. Laplane, [arXiv:2409.08827](https://arxiv.org/abs/2409.08827) (2024).

[18] R. P. Middlemiss, A. Samarelli, D. J. Paul, J. Hough, S. Rowan, G. D. Hammond, and J. T. Wright, *Nature* **531**, 614 (2016).

[19] S. Tang, H. Liu, S. Yan, X. Xu, W. Wu, J. Fan, J. Liu, C. Hu, and L. Tu, *Microsystems and Nanoengineering* **5**, 45 (2019).

[20] A. Mustafazade, M. Pandit, C. Zhao, G. Sobreviela, Z. Du, P. Steinmann, X. Zou, R. T. Howe, and A. A. Seshia, *Scientific Reports* **10**, 10415 (2020).

[21] B. Kirkendall, Y. Li, and D. Oldenburg, *IEEE Transactions on Geoscience and Remote Sensing* **45**, 1786 (2007).

[22] L. Wu and J. Tian, *Journal of Geophysics and Engineering* **7**, 410 (2010).

[23] Y.-W. Kwon, J.-K. Ahn, J. Lee, and C.-H. Lee, in *IGARSS 2020 - 2020 IEEE International Geoscience and Remote Sensing Symposium* (2020) pp. 6635–6637.

[24] See Supplemental Material for further details about the theoretical properties of gravitational communication, analytical modelling and experimental considerations. Contains Refs. [25, 27, 38, 39].

[25] S. Ramo, J. Whinnery, and T. Van Duzer, *Fields and Waves in Communication Electronics* (Wiley, 1994).

[26] C. E. Shannon, *Bell System Technical Journal* **27**, 379 (1948).

[27] *Instruction Manual: Model G and D Gravity Meters*, LaCoste and Romberg, 4807 Spicewood Springs Road, Austin, Texas, USA (1997).

[28] J. Senior and M. Jamro, *Optical Fiber Communications: Principles and Practice*, 3rd ed. (Pearson Education, 2009).

[29] We verified that there was a negligible change in the local magnetic field at the sensor's location when the counterweight was moved, as this could in principle affect the gravimeter's steel spring [24].

[30] P. Massoud Salehi and J. Proakis, *Digital Communications*, 5th ed. (McGraw-Hill Education, 2008).

[31] *CG-6 Autograv™ Gravity Meter Operation Manual*, Scintrex, 222 Snidercroft Road, Concord, ON, Canada, L4K 2K1 (2018).

[32] O. Francis, *Journal of Geodesy* **95**, 116 (2021).

[33] Combat Vehicles: Challenger 2, <https://www.army.mod.uk/learn-and-explore/equipment/combat-vehicles/challenger-2/>, accessed: 20th Aug 2025.

[34] S.-W. Chiow, T. Kovachy, H.-C. Chien, and M. A. Kasevich, *Physical Review Letters* **107**, 130403 (2011).

[35] A. HosseiniArani, M. Schilling, Q. Beauflis, A. Knabe, B. Tennstedt, A. Kupriyanov, S. Schön, F. Pereira dos Santos, and J. Müller, *Advances in Space Research* **74**, 3186 (2024).

[36] Voyager 1 and 2 spacecraft, <https://science.nasa.gov/mission/voyager/spacecraft/>, accessed: 15th Oct 2025.

[37] H. Kater, *Philosophical Transactions of the Royal Society of London* **108**, 33 (1818).

[38] I. M. Longman, *Journal of Geophysical Research* (1896-1977) **64**, 2351 (1959).

[39] X. Li and M. Chouteau, *Surveys in Geophysics* **19**, 339 (1998).

Supplemental Material: Unblockable Communication With Gravity

Andrew J. Groszek ,^{1,2} Charles W. Woffinden ,^{1,2} Michael D. Harvey ,^{2,3} Andrew G. White ,² and Matthew J. Davis ,²

¹*These authors have contributed equally to this work and share first authorship.*

²*Australian Research Council Centre of Excellence for Engineered Quantum Systems,
School of Mathematics and Physics, University of Queensland, St. Lucia, QLD 4072, Australia.*

³*Quantum Australia, School of Mathematics and Physics,
University of Queensland, St. Lucia, QLD 4072, Australia.*

I. PROPERTIES OF GRAVITATIONAL COMMUNICATION

A. Optimisation

In the main text, we discuss the gravitational signal strength $\Delta\mathbf{g} = \mathbf{g}(\mathbf{r}_1) - \mathbf{g}(\mathbf{r}_0)$ Alice generates as she moves a point mass M between two positions \mathbf{r}_0 and \mathbf{r}_1 [where $\mathbf{g}(\mathbf{r}) = (GM/r^2)\hat{\mathbf{r}}$]. Here we consider how Alice can optimise her transmission by choosing positions that maximise this signal.

Her choices will depend on several factors. Firstly, many gravimeters only measure along a single axis $\hat{\mathbf{n}}$ (usually the vertical, $\hat{\mathbf{z}}$), in which case Alice should aim to maximise $\Delta g_n \equiv \Delta\mathbf{g} \cdot \hat{\mathbf{n}}$. If, on the other hand, Bob is in possession of a full three-axis sensor, Alice should instead maximise $|\Delta\mathbf{g}|$. Secondly, since we are assuming that Alice is confined to a shielded room (see main text), her options for \mathbf{r}_0 and \mathbf{r}_1 will be naturally constrained.

As a benchmark, we first consider an idealised case where the mass is free to move anywhere around the gravimeter on the surface of a sphere with radius R . Here, the strongest three-axis signal will be achieved by moving the mass between two diametrically opposite points on the sphere, i.e. $\mathbf{r}_0 = -\mathbf{r}_1$, giving a maximum signal of $|\Delta\mathbf{g}| = 2GM/R^2$. This same signal can also be achieved with a single-axis sensor, provided the positions are also aligned with the measurement axis, i.e. $\mathbf{r}_0 = -\mathbf{r}_1 = \pm R\hat{\mathbf{n}}$ (if $\hat{\mathbf{n}}$ is rotated from this orientation, the signal will be reduced by a factor of $\hat{\mathbf{r}}_0 \cdot \hat{\mathbf{n}}$).

In the scenario envisioned in Fig. 1 of the main text, where a vertical wall separates the mass and the gravimeter, this ideal optimisation strategy is not possible. Instead, we consider Alice's mass to be constrained to a vertical line parallel to the wall, a fixed perpendicular distance d from the gravimeter, and with variable vertical position z [see Fig. S1(a)]. In this configuration, the optimal solution for a three-axis sensor is to move the mass from $z_0 = 0$ (the closest point to the gravimeter) to $z_1 \rightarrow \pm\infty$, giving $|\Delta\mathbf{g}| = GM/d^2$. This is a factor of two worse than the ideal case above (taking $R = d$), owing to the restriction that the mass remains on one side of the sensor.

For a single-axis sensor, the situation is more complicated. In the remainder of this section, we wish to determine the positions z_0 and z_1 that maximise Δg_n for a given sensor direction $\hat{\mathbf{n}}$. Trivially, the strongest signal will be obtained when $\hat{\mathbf{n}}$ points directly towards the wall [along the direction $\hat{\mathbf{x}}$ depicted in Fig. S1(a)]. In this case, the optimal mass positions and signal are the same as for the three-axis sensor. However, since most sensors measure vertical gravity (i.e. $\hat{\mathbf{n}} = \hat{\mathbf{z}}$), the natural question is how much sensitivity is lost as $\hat{\mathbf{n}}$ is rotated

from the horizontal ($\hat{\mathbf{x}}$) to the vertical ($\hat{\mathbf{z}}$) axis.

We first express the vertical position of the mass in terms of its polar angle θ from the sensor (related to its height via $z = d/\tan\theta$). It is convenient to parametrise $\hat{\mathbf{n}}$ in terms of a polar angle $0^\circ \leq \eta < 180^\circ$ [as shown in Fig. S1(a)] and an azimuthal angle $0^\circ \leq \zeta < 360^\circ$ (the rotation around $\hat{\mathbf{z}}$, which we include for generality). The detected gravitational pull towards the mass, $g_n = \mathbf{g} \cdot \hat{\mathbf{n}}$, can then be written in terms of these three angles:

$$g_n(\theta, \eta, \zeta) = \frac{GM}{d^2} \sin^2 \theta (\cos \theta \cos \eta + \sin \theta \sin \eta \cos \zeta). \quad (1)$$

This function is plotted in terms of θ and η in Fig. S1(b) for $\zeta = 0$. For a given sensor angle η , there are two extremal values of the gravitational signal—a maximally positive and a maximally negative value. These occur at mass angles

$$\theta_{\pm}^*(\eta) = \eta/2 \pm \arccos(-\cos(\eta)/3)/2 \quad (2)$$

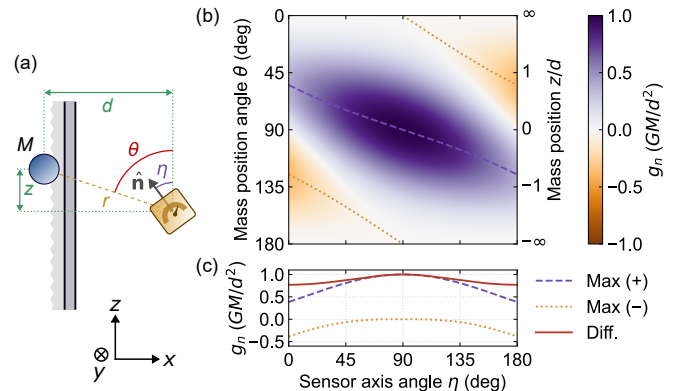


Figure S1. Signal optimisation with a vertically constrained mass and a single-axis gravimeter. (a) Setup with the mass allowed to move vertically on one side of a wall, and the sensor on the other side. The mass position can be parametrised by either its vertical position z or polar angle θ . The sensor's measurement axis $\hat{\mathbf{n}}$ is expressed in terms of a polar angle η (measured relative to $\hat{\mathbf{z}}$) and an azimuthal angle ζ in the xy -plane (measured relative to $\hat{\mathbf{x}}$; not shown). (b) The detected gravitational acceleration $g_n(\theta, \eta, \zeta = 0)$ [Eq. (1)] as a function of sensor axis angle η and mass angle θ (or mass position z ; right vertical axis). The purple dashed (orange dotted) line shows the location of the maximally positive (negative) value of g_n at each value of η . (c) The extremal g_n values identified in (b), plotted as a function of sensor polar angle η . The solid red line shows the difference between these extremal values, corresponding to the optimal signal Δg_n for a given η .

(modulo 180°). Here, the * notation identifies these as extremal points, and \pm denotes the maximally positive (+) and maximally negative (−) position. These extrema are identified in Fig. S1(b) with a purple dashed and orange dotted line, respectively. Note that, because we have assumed the sensor always points towards the wall, the maximally positive signal is larger in magnitude than the maximally negative signal for all η . If we instead tilted the sensor away from the wall by a polar angle η , the situation would reverse.

Figure S1(c) shows these extremal values as a function of η (using the same line types). Also shown in this frame is the difference between the two curves, corresponding to the largest attainable value of Δg_n for a given sensor angle η (solid red line). In practice, this is obtained by choosing mass positions $\theta_0 = \theta_+^*$ and $\theta_1 = \theta_-^*$. Evidently, the global maximum of the signal is obtained when $\eta = 90^\circ$ (i.e. the sensor pointing along $\hat{\mathbf{x}}$, as identified earlier). In this case, the optimal mass positions are $\theta_+^* = 90^\circ$ and $\theta_-^* = 0^\circ$ or 180° , as identified above [see Fig. S1(b)]. As the sensor is rotated towards $\hat{\mathbf{z}}$, the optimal signal reduces, until it reaches a minimum at $\eta = 0^\circ$ (or equivalently, $\eta = 180^\circ$). Remarkably, though, this signal is only $\approx 23\%$ smaller than the global maximum (i.e. $\approx 0.77GM/d^2$), despite the sensor now pointing parallel to the wall. In this case, the optimal choice of mass angles is $\theta_+^* \approx 55^\circ$, $\theta_-^* \approx 125^\circ$ [from Eq. (2)]—or equivalently, $z_\pm^* \approx \pm 0.7d$ (as stated in the main text). We therefore conclude that the measurement axis of the sensor makes only a modest difference to the overall sensitivity achievable in this configuration.

However, we note that the movement distance of $\approx 1.4d$ required to achieve this optimal signal is larger than the transmission length d , which may be unrealistic in practice. Taking instead the limit of a small mass movement $|z_0| \ll d$ symmetric around $z = 0$ (i.e. $z_0 = -z_1$), Eq. (1) gives $\Delta g_z \approx (2z_0/d)(GM/d^2)$ (still taking $\eta = 0^\circ$). The signal will therefore be a factor of $2z_0/d$ smaller than the global maximum.

For completeness, we also consider the effect of nonzero azimuthal angle ζ [rotating $\hat{\mathbf{n}}$ into or out of the page in Fig. S1(a)]. This can only ever reduce the signal, since the mass is confined to the xz -plane, and should therefore be avoided. As ζ increases from 0°, the central peak in Δg_n [solid line in Fig. S1(c)] reduces in value, eventually becoming a dip, while the endpoints at $\eta = 0^\circ$ and $\eta = 180^\circ$ remain fixed (because the azimuthal angle is irrelevant when the sensor is pointing along $\hat{\mathbf{z}}$). For $\zeta = \eta = 90^\circ$, the signal vanishes completely, because the sensor is pointing along $\hat{\mathbf{y}}$, and hence it will always be perpendicular to the mass.

B. Derivation of antenna signal

In the main text, we consider the transmission pattern produced by a gravitational antenna, formed by moving a point mass M between two vertical positions $+\Delta z$ and $-\Delta z$ [see Fig. 2(a) of the main text]. An observer at position \mathbf{r} will detect a change in gravitational acceleration as the mass is moved between the upper (1) and lower (0) positions, given by:

$$\Delta \mathbf{g}(\mathbf{r}) = \mathbf{g}_1(\mathbf{r}) - \mathbf{g}_0(\mathbf{r}) = GM \left[\frac{\mathbf{r}_1 - \mathbf{r}}{|\mathbf{r}_1 - \mathbf{r}|^3} - \frac{\mathbf{r}_0 - \mathbf{r}}{|\mathbf{r}_0 - \mathbf{r}|^3} \right], \quad (3)$$

where $\mathbf{r}_1 = \Delta z \hat{\mathbf{z}} = -\mathbf{r}_0$. This signal is confined to the 2D plane containing \mathbf{r}_0 , \mathbf{r}_1 and \mathbf{r} , which we refer to as the xz -plane without loss of generality. The position of the gravimeter in this plane can then be expressed in polar coordinates as $\mathbf{r} = (r, \alpha)$, in which case the horizontal and vertical components of the above expression are, respectively:

$$\begin{aligned} \Delta g_x(\mathbf{r}) &= GM \left(-\frac{r \sin \alpha}{\delta_+^3} + \frac{r \sin \alpha}{\delta_-^3} \right), \\ \Delta g_z(\mathbf{r}) &= GM \left(\frac{\Delta z - r \cos \alpha}{\delta_+^3} + \frac{\Delta z + r \cos \alpha}{\delta_-^3} \right), \end{aligned} \quad (4)$$

where $\delta_\pm = (r^2 + \Delta z^2 \pm 2\Delta z r \cos \alpha)^{1/2}$. Figure S2 presents normalised polar plots of both the horizontal signal Δg_x [panel (a)] and the magnitude of the total signal $|\Delta \mathbf{g}| = (\Delta g_x^2 + \Delta g_z^2)^{1/2}$ [panel (b)] as a function of polar angle α , at multiple values of $r/\Delta z$ [the vertical signal Δg_z is shown in Fig. 2(b) of the main text]. In the near- and far-field limits ($r \ll \Delta z$ and $r \gg \Delta z$, respectively), Δg_x consists of four lobes, centred at angles $\alpha = \{45^\circ, 135^\circ, 225^\circ, 315^\circ\}$. This horizontal signal is unchanged upon exchanging $r \leftrightarrow \Delta z$, up to a rescaling by $r/\Delta z$ [see Eq. (4)]; as such, the normalised plots of Δg_x are symmetric about $r/\Delta z = 1$. An observer in the far-field and an observer near the origin therefore see equivalent Δg_x patterns. However, the Δg_x component is small in magnitude compared to Δg_z , and therefore has only a minor impact on the shape of the overall signal $|\Delta \mathbf{g}|$. This is evident from Fig. S2(b), which looks qualitatively similar to the plot of Δg_z in Fig. 2(b) of the main text.

Taking the far-field limit ($r \gg \Delta z$), Eqs. (4) reduce to:

$$\begin{aligned} \Delta g_x &\approx 6\Delta z \frac{GM}{r^3} \sin(\alpha) \cos(\alpha), \\ \Delta g_z &\approx 6\Delta z \frac{GM}{r^3} \left(\cos^2(\alpha) + \frac{1}{3} \right). \end{aligned} \quad (5)$$

From these expressions, the far-field half-power beam widths (HPBWs) of each component can be determined, which characterise the angular spread of the signal. These are: 45° (horizontal, Δg_x), $2 \arccos(1/3^{1/2}) \approx 109^\circ$ (vertical, Δg_z), and

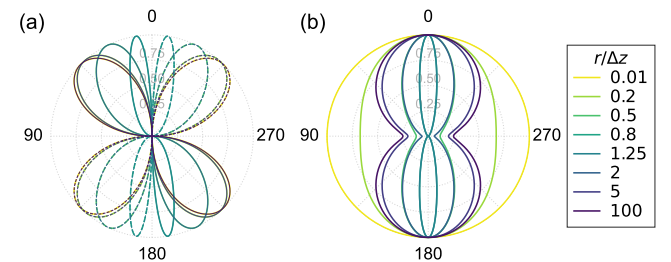


Figure S2. Polar plots of the normalised signal from the gravitational dipole antenna configuration shown in Fig. 2(a) of the main text, as a function of polar angle α from the antenna's axis. Here we show (a) the horizontal signal Δg_x , and (b) the total signal $|\Delta \mathbf{g}|$ [the vertical signal Δg_z is shown in Fig. 2(b) of the main text]. The legend denotes the value of $r/\Delta z$ for each curve, and each curve is normalised to the largest value for that radius. In (a), solid (dashed) lines denote a positive (negative) signal. Note that all patterns are symmetric with respect to the observer's azimuthal angle.

$\arccos(-3/5) \approx 127^\circ$ (total, $|\Delta\mathbf{g}|$). Therefore, measuring $|\Delta\mathbf{g}|$, rather than Δg_z , serves to widen the antenna lobes slightly in the far-field limit, as can be seen by comparing Fig. S2(b) and Fig. 2(b) of the main text. The Δg_z and $|\Delta\mathbf{g}|$ HPBWs are somewhat greater than the $\approx 78^\circ$ of the electromagnetic half-wave dipole antenna, whose radiation pattern is given by $\sim \cos^2[(\pi/2) \cos \alpha] / \sin^2 \alpha$ [1] [see Fig. 2(b) of the main text]. The gravitational antenna would therefore typically be considered less efficient, as it transmits signal over a wider range, including partially in the perpendicular direction.

C. Robustness to jamming and spoofing

If Bob has access to a three-axis gravimeter, he can use the full vector information $\Delta\mathbf{g}$ to mitigate against jamming and spoofing attacks from a malicious actor, Mallory. If Mallory attempts to jam Alice's true signal by moving one or more other masses nearby to Bob, the signal $\Delta\mathbf{g} \cdot \hat{\mathbf{n}}$ from a single-axis sensor (with sensing direction $\hat{\mathbf{n}}$) could become overwhelmed by Mallory's signal. A three-axis sensor, on the other hand, would detect the jamming signal in all three vector components, and this could provide valuable additional information. For example, if the true mass is known to be moving only in a single axis, the malicious signal in the perpendicular components would be correlated with the noise in the direction of the true mass, allowing Alice to isolate this signal and remove it. In more general situations, isolating the true signal becomes a nontrivial inverse problem, although it may be solvable if enough information about Alice's true signal is known (e.g. the expected amplitude or frequency).

A three-axis sensor would also make any attempts at spoofing Alice's signal (i.e. producing false 0s and 1s) exceedingly difficult, because Mallory's mass would have to produce the same vector $\Delta\mathbf{g}$ at Bob's detector as Alice's true mass. This would only be possible if Mallory's mass is placed colinear with both the sensor and Alice's mass in each of the 0 and

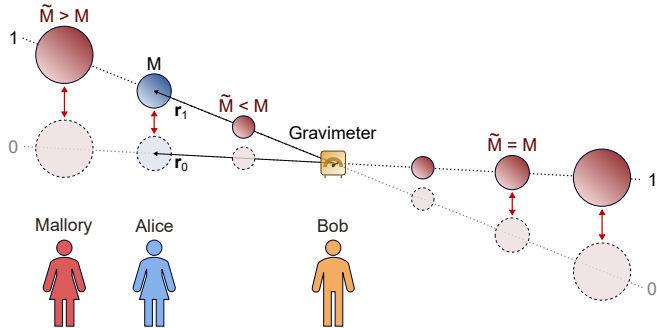


Figure S3. Schematic demonstrating Mallory's attempts to spoof Alice's signal using a second mass \tilde{M} . If Alice moves her mass M from \mathbf{r}_0 to \mathbf{r}_1 to produce a signal $\Delta\mathbf{g}$ at Bob's gravimeter, Mallory would need to position their mass \tilde{M} along the same radial vectors, either closer (if $\tilde{M} < M$) or further away (if $\tilde{M} > M$). Mallory could also position themselves on the opposite side of the detector to Alice, but in that case would need to swap the 0 and 1 positions in order to produce the same $\Delta\mathbf{g}$ as Alice.

1 positions, as outlined in Fig. S3. If Mallory is on the same side of the sensor as Alice with their own mass \tilde{M} , they would need to position themselves at $\tilde{\mathbf{r}}_i = (\tilde{M}/M)^{1/2} \mathbf{r}_i$, for $i = \{0, 1\}$ (left side of Fig. S3). If Mallory instead tries to spoof the signal from the opposite side of the sensor to Alice (right side of Fig. S3), the signals produced would be $-\mathbf{g}(\mathbf{r}_0)$ and $-\mathbf{g}(\mathbf{r}_1)$ at $\tilde{\mathbf{r}}_0$ and $\tilde{\mathbf{r}}_1$, respectively. In the case where Bob is using a relative gravimeter, Mallory could still spoof the signal from this side of the gravimeter by reversing these positions, resulting in the same $\Delta\mathbf{g}$ as Alice. If, on the other hand, Bob is using an absolute gravimeter capable of directly measuring the full gravity vectors $\mathbf{g}(\mathbf{r}_0)$ and $\mathbf{g}(\mathbf{r}_1)$, Mallory could only successfully spoof Alice's signal from the same side of the sensor. Given that this communication scheme is restricted to relatively short range applications, Mallory (along with their large mass \tilde{M}) may have a difficult time remaining unnoticed during these attempts, anyway.

II. ANALYTICAL MODEL

We have constructed a model of the experimental configuration to estimate the gravitational signal we expect to observe at the location of the gravimeter. The counterweight is approximated to be a 3D rectangular prism of uniform of density $\rho = 7300(200) \text{ kg m}^{-3}$ and volume $L_x \times L_y \times L_z$, with $L_x = 0.205(5) \text{ m}$, $L_y = 0.82(1) \text{ m}$, and $L_z = 1.47(4) \text{ m}$. We position its COM at $x = 0.56(3) \text{ m}$, $y = 0.00(5) \text{ m}$, and allow it to move along the vertical (z) axis. (Section III B describes how these measurements have been obtained.) At each vertical position, we calculate the gravitational field by integrating Newton's law of gravitation over the density distribution:

$$\mathbf{g}(\mathbf{r}_s) = -G \int_{\mathcal{V}} d^3 \mathbf{r}' \frac{\rho(\mathbf{r}')}{|\mathbf{r}_s - \mathbf{r}'|^3} (\mathbf{r}_s - \mathbf{r}'), \quad (6)$$

where \mathcal{V} is the region containing nonzero density, and \mathbf{r}_s is the location of the sensor. For a rectangular prism of fixed density

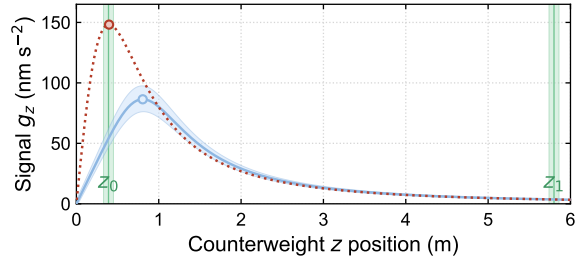


Figure S4. Analytical model of the vertical gravitational acceleration g_z due to the counterweight (blue solid line), as a function of the z -position of its centre of mass, relative to the gravimeter. Shading around the curve denotes one standard deviation error arising from the uncertainty in the counterweight size and density, as well as the distance to the sensor. Vertical lines indicate z_0 and z_1 , the lower and upper positions of the counterweight, respectively. The shaded regions show one standard deviation error in these positions. A point mass approximation of the signal is also shown (red dotted line). The maximal signal, corresponding to the position z^* , is indicated on each line with a circle.

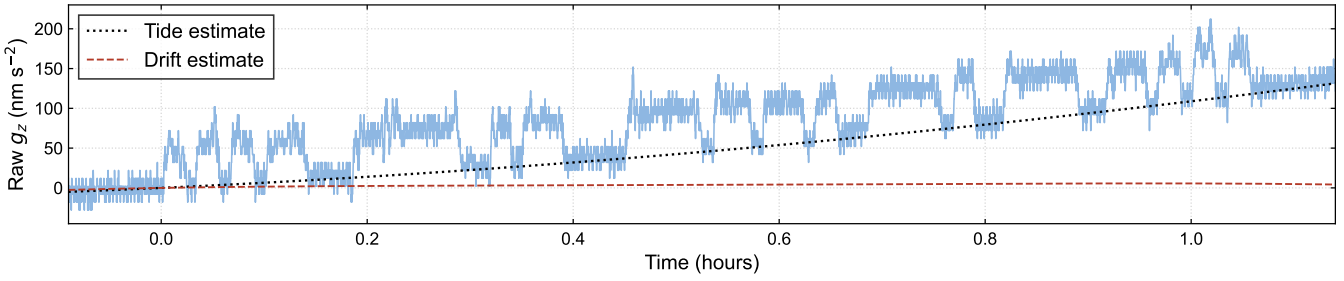


Figure S5. Raw gravimetry signal g_z over the transmission sequence (solid line), as well as the Longman tide prediction [2] (black dotted line) and an estimate of the drift (red dashed line). Note that the gravimeter outputs a relative measurement, meaning that the overall offset of the data is arbitrary. Note also the sign convention of the data, whereby a positive change in g_z corresponds to an increase in downward acceleration.

ρ contained within the region $x_1 \leq x \leq x_2$, $y_1 \leq y \leq y_2$, $z_1 \leq z \leq z_2$, the resulting expression for \mathbf{g} can be written analytically as [3]:

$$\mathbf{g}(\mathbf{r}_s) = G\rho \sum_{k,l,m=1}^2 (-1)^{k+l+m} \mathbf{F}_{klm}(\mathbf{r}_s). \quad (7)$$

The x -component of \mathbf{F} can be written:

$$(F_{klm})_x = \Delta y_l \log(\Delta z_m + \Delta r_{klm}) + \Delta z_m \log(\Delta y_l + \Delta r_{klm}) - \Delta x_k \arctan\left(\frac{\Delta y_l \Delta z_m}{\Delta x_k \Delta r_{klm}}\right), \quad (8)$$

where $\Delta x_k = x_k - x_s$, $\Delta y_l = y_l - y_s$, $\Delta z_m = z_m - z_s$, and $\Delta r_{klm} = (\Delta x_k^2 + \Delta y_l^2 + \Delta z_m^2)^{1/2}$. The y (z) component of \mathbf{F} can then be obtained by permuting $\Delta x_k \rightarrow \Delta y_l$, $\Delta y_l \rightarrow \Delta z_m$, $\Delta z_m \rightarrow \Delta x_k$ once (twice).

Figure S4 shows the vertical gravitational signal g_z obtained from the model (solid blue line), with uncertainty indicated by the shading. At large distances, the gravitational pull is weak, but increases as the counterweight moves downward. However, past the peak at ≈ 0.8 m (identified with a circle), the signal starts to drop towards zero as the gravitational field becomes predominantly along the x -axis. This peak corresponds to the optimal position z_+^* discussed in Sec. IA. In Fig. S4, we also show the signal predicted for a point mass with the same total mass as the counterweight, located at the position of its COM (dotted line). As expected, the two curves agree in the far-field, where the distributed density begins to look point-like. However, when the counterweight is closer to the sensor, the point mass curve produces a much stronger signal, and the optimal position shifts to $z_+^* \approx 0.4$ m. This highlights the benefits that could be realised if the mass was made denser (e.g. compacted into a sphere).

The experimental values for the lower and upper positions of the counterweight (z_0 and z_1 , respectively) are indicated in Fig. S4 with vertical lines (shading denotes the uncertainty in these values). (See Sec. III B for details regarding how these positions were obtained.) According to the distributed counterweight model, the expected signals at each location are $54(15)$ nm s $^{-2}$ (lower) and $3.6(3)$ nm s $^{-2}$ (upper), giving a difference of $\Delta g_z = 50(15)$ nm s $^{-2}$. This value agrees well with the experimentally observed signal of ≈ 50 nm s $^{-2}$.

III. EXPERIMENTAL CONSIDERATIONS

A. Raw gravitational signal

The raw vertical gravitational signal g_z detected by the gravimeter over the experimental sequence is plotted in Fig. S5. The dotted black line shows the Longman Earth tide prediction [2], which captures the majority of the signal drift over time. We also account for sensor drift and any second order tidal effects with an additional quartic fit (red dashed line) to the data after subtracting the tide prediction. This fit includes the background measurements before and after the bit sequence, as well as the two strings of ≥ 3 consecutive 0s within the sequence. Subtracting these two contributions from the raw data give the corrected data presented in Fig. 4 of the main text.

B. Estimation of counterweight geometry and mass

To determine the counterweight COM z -position relative to the gravimeter in its lower position in the experiment, we used a laser distance meter (LDM) and purpose-built pendulum theodolite, mounted to a tripod (see left side of Fig. S6). The pendulum theodolite consisted of a fishing line with a mass on the end, attached to the centre of a protractor. A laser pointer was also mounted along the edge of the protractor, directed along the $0-180^\circ$ line. The theodolite was first aligned such that the laser pointed to the top of the counterweight (solid red line in Fig. S6), before being rotated until the laser reached the bottom of the counterweight (dashed red line). As it was rotated, the pendulum remained vertical due to gravity, allowing a measurement of the angles α_1 and α_2 relative to this reference (see Fig. S6). We then attached the LDM to the centre of the theodolite, enabling us to measure the distance d_1 from this point to the top of the counterweight (the LDM could not provide a reliable measurement of the distance d_2 to the bottom of the counterweight, due to poor reflectance). Using these measurements, as well as the measured height of the theodolite, trigonometry was used to determine the counterweight's vertical length, $L_z = 1.47(4)$ m. The counterweight's centre-point (assumed to be its COM) was

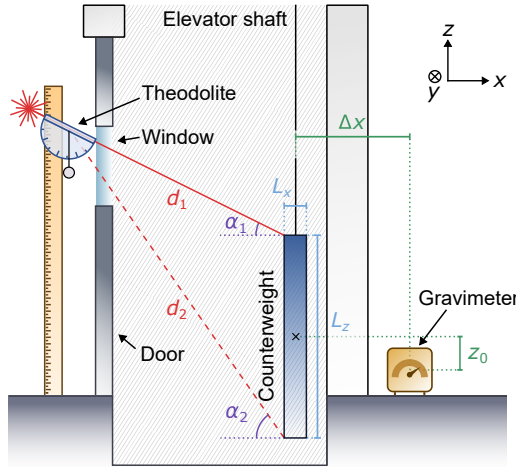


Figure S6. Schematic diagram of the experimental setup and measurement scheme for the elevator counterweight dimensions, while in the lower position (not to scale). The left side shows the combined laser distance meter and theodolite, used for measuring the angle α_1 (α_2) to the top (bottom) of the counterweight, as well as the distance d_1 (d_2 could not be measured; see text). The counterweight height L_z and vertical position z_0 obtained using this method are indicated, as well as the horizontal depth L_x and distance to the gravimeter Δx .

also estimated from this method to be at a vertical position $z_0 = 0.39(6)$ m above the gravimeter (see Fig. S6). Building plans informed us that the elevator moves a distance 5.41 m between the upper and lower levels, and hence the upper position of the counterweight was estimated to be $z_1 = 5.80(6)$ m.

The depth L_x and width L_y could not be estimated using this method, due to a lack of absolute horizontal reference. Fortunately, shortly after completing the experiment, a technician performing an elevator service was kind enough to provide us with measurements of $L_x = 0.205(5)$ m, $L_y = 0.82(1)$ m.

To obtain the horizontal distance Δx between the counterweight and the gravimeter, we needed an estimate of the wall thickness (the technician also provided a measurement of the distance between the counterweight and the wall). To this end, we conducted a survey with a tape measure and the LDM from our reference point at the front of the elevator shaft to the gravimeter, via a hallway next to the elevator shaft. This gave a wall thickness of 0.27(2) m, consistent with a nearby wall in the same building that we could measure directly. We therefore estimated the total separation to be $\Delta x = 0.56(3)$ m.

Finally, from the counterweight's measured dimensions, we estimated its mass to be 1800(200) kg, assuming a uniform density of 7300(200) kg m⁻³. This density is typical of grey cast iron—the material of choice for mid 20th-century lift counterweights.

C. Influence of magnetic fields

Because the gravimeter uses a steel spring, measurements could in principle be influenced by magnetic fields. To mitigate this, the sensor contains two layers of μ -metal shielding [4]. However, this shielding is only effective up to a saturation point, and provides a finite attenuation factor, rather than complete suppression. Sufficiently strong fields could therefore still give rise to erroneous gravitational measurements.

To verify that the experimentally observed signal was not due to the iron counterweight's magnetic field, we repeated the experiment with an additional layer of magnetic shielding around the gravimeter. A magnetometer mounted on the side of the gravimeter confirmed that this additional shielding reduced the residual magnetic field by a factor of ~ 10 . However, when the counterweight was moved between its upper and lower positions with this shielding in place, the obtained gravitational signal was unchanged. We therefore conclude that the measured signal is indeed gravitational in origin.

D. Allan deviation

Figure S7 shows the Allan deviation of the gravimeter, calculated from the 25 min of background reading obtained before beginning the experimental sequence. Integrating using the raw data (circles) gives a minimum uncertainty of ≈ 2 nm s⁻² at ≈ 30 s, before this value begins to increase again due to the influence of tides and drift. If we instead calculate the Allan deviation of the tide- and drift-corrected signal over the same window (diamonds), the uncertainty continues to decrease, and appears to minimise after ≈ 100 s of integration, with a value of ≈ 1.4 nm s⁻². Both curves appear to roughly follow $\sim t^{-1/2}$ scaling for the first ≈ 20 s, although there are significant temporal oscillations observed. These may arise from oscillations within the building structure, although this has not been verified.

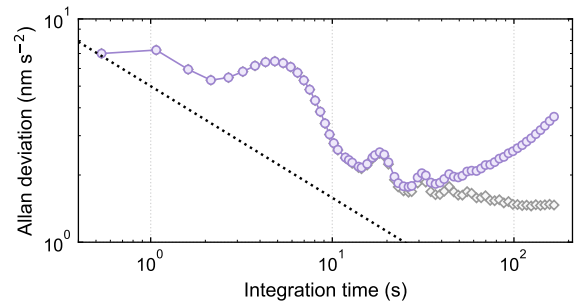


Figure S7. Allan deviation of the sensor, calculated from the ≈ 25 min background measurement obtained before the experimental transmission sequence. Purple circles (grey diamonds) show the Allan deviation calculated using the raw data (tide- and drift-corrected data). The dotted line shows a $t^{-1/2}$ power-law, for comparison.

- [1] S. Ramo, J. Whinnery, and T. Van Duzer, *Fields and Waves in Communication Electronics* (Wiley, 1994).
- [2] I. M. Longman, *Journal of Geophysical Research (1896-1977)* **64**, 2351 (1959).
- [3] X. Li and M. Chouteau, *Surveys in Geophysics* **19**, 339 (1998).
- [4] *Instruction Manual: Model G and D Gravity Meters*, LaCoste and Romberg, 4807 Spicewood Springs Road, Austin, Texas, USA (1997).